Inhalation Toxicology, 19:1155–1165, 2007

ISSN: 0895-8378 print / 1091-7691 online
DOI: 10.1080/08958370701665525

informa
healthcare

Deposition of Inhaled Wood Dust in the Nasal Cavity

Z. F. Tian, K. Inthavong, and J. Y. Tu

School of Aerospace, Mechanical and Manufacturing Engineering, RMIT University, Bundoora, Victoria, Australia

Detailed deposition patterns of inhaled wood dust in an anatomically accurate nasal cavity were investigated using computational fluid dynamics (CFD) techniques. Three wood dusts, pine dust, heavy oak dust, and light oak dust, with a particle size distribution generated by machining (Chung et al., 2000), were simulated at an inhalation flow rate of 10 L/min. It was found that the major particle deposition sites were the nasal valve region and anterior section of the middle turbinate. Wood dust depositing in these regions is physiologically removed much more slowly than in other regions. This leads to the surrounding layer of soft tissues being damaged by the deposited particles during continuous exposure to wood dust. Additionally, it was found that pine dust had a higher deposition efficiency in the nasal cavity than the two oak dusts, due to the fact that it comprises a higher proportion of larger sized particles. Therefore, this indicates that dusts with a large amount of fine particles, such as those generated by sanding, may penetrate the nasal cavity and travel further into the lung.

INTRODUCTION

Wood dust is one of the most common organic dusts to which humans are exposed to due to the extensive use of wood for construction material and furniture (Enarson & Chan-Yeung, 1990). The International Agency for Research on Cancer estimated that at least 2 million people in the world are exposed to wood dust occupationally (IARC/WHO, 1995). Exposure is common in many types of work, especially in the primary wood industries such as logging, lumber mills, and pulp mills and even more so in secondary wood industries such as cabinet making, furniture manufacture, wood pattern and work shops, and other manufacturing industries (Enarson & Chan-Yeung, 1990).

Although trees are classified as either gymnosperms (having needle-like leaves) or as angiosperms (having broad leaves and is deciduous), they are more often classified as hardwoods and softwoods in practice. Hardwoods are primarily angiosperms such as oak, while softwoods are gymnosperms such as pine. The terms refer to the species and not necessarily the hardness, although hardwoods tend to be denser than softwoods. The processing of the raw timber from the use of high-powered reciprocating tools such as sanding and sawmills generates large quantities of fine, inhalable wood dust. Direct contact with the wood dust leads to inhalation of the particles via the nasal cavity. It is not surprising, then, that significant health effects have resulted from direct contact of the inhaled wood dusts with tissues of the respiratory tract. While ingestion is also common, no health effects have been reported.

The effects from deposited wood particles in the nasal cavity have been found to be a potential cause of respiratory diseases including allergic rhinitis, nasal mucociliary stasis, and asthma. Moreover, wood dust has been known to be a human carcinogen, and studies of occupations associated with wood dust exposure have revealed strong and consistent links to nasal cavity cancer and paranasal sinus cancer (National Toxicology Program, 2005), although the actual carcinogenic agent, either naturally in the wood or from a processing additive, is not clearly known. However, the particulate nature of the wood dust is believed to contribute toward associated carcinogenesis, since dust generated by machining usually comprises a high proportion of particles that are deposited in the nasal cavity (National Toxicology Program, 2005). The physiological response such as clearance of deposited depends on their deposition site in the nasal cavity (Fry & Black, 1973; Cheng et al., 1996). There are two major clearance mechanisms of inhaled wood particles in the nasal cavity: the mucociliary mechanism and by physical means. Particles deposited on the ciliated epithelium of the nose are cleared by the mucociliary action, i.e., cilia beating that moves the mucus secretion toward the pharynx. The anterior third of the nose is not covered by ciliated epithelium, but rather cutaneous epithelium that is like the skin. The clearance mechanism of deposited wood particles in this region is thought to occur by physical means such as sneezing, wiping, and blowing (Swift & Kesavanathan, 1996),

Received 20 June 2007; accepted 8 August 2007.

Address correspondence to Prof Jiyuan Tu, School of Aerospace, Mechanical, and Manufacturing Engineering, RMIT University, PO Box 71, Bundoora Vic 3083, Austrália. E-mail: Jiyuan.Tu@rmit.edu.au

which lead to a slower clearance than in the ciliated epithelium region.

Particle deposition in the human nasal cavity has been studied by in vivo measurements (Pattle, 1961; Hounam et al., 1971; Heyder & Rudolf, 1977; Keck et al., 2000; Wiesmiller et al., 2003; and many others) and in-vitro tests (Swift, 1991; Guilmette et al., 1994; Zwartz & Guildmore, 2004; Häußermann et al., 2002; Kelly et al., 2004; and many others). Through these studies, it was found that particle deposition in the nasal cavity is strongly influenced by three major factors: (1) particle morphology, including particle diameter, shape, and density; (2) physiological factors such as respiratory ventilation and pattern; and (3) nasal morphological factors such as airway size and shape (Cheng et al., 1996).

Through the advances in computing power and numerical algorithms, computational fluid dynamics (CFD) simulations have evolved into a feasible alternative to complement experimental data. For example CFD simulations for airflow patterns (Keyhani et al., 1995; Subramanian et al., 1998; Finck et al. 2006) have complemented experimental results (Hahn et al., 1993) by confirming regions of vortices within the nasal vestibule, the olfactory region, and posterior to the nasal valve. Simulations for particle deposition in the nasal cavity, however, are fewer in number, though many CFD studies of particle deposition in the oral airway have been reported (Stapleton et al., 2000; Martonen et al., 2002; Zhang et al., 2002). Inthavong et al. (2006) numerically studied particle deposition in a realistic human nasal cavity under conditions related to pharmaceutical nasal spray applications. Particles in the range of 10 μm to 50 μm subjected to a breathing flow rate of 20 L/min were found to deposit in the anterior third of the nasal cavity. This was attributed to the injected particles existing in a high inertial regime. Schroeter et al. (2006) employed CFD to analyze particle deposition in the nasal cavity, particularly in the turbinate and olfactory region. They found high deposition in the nasal valve region, medium deposition in the turbinate region, and very low deposition in the olfactory region. Shi et al. (2007) evaluated the effects of wall roughness on the deposition of particles in a human nasal cavity numerically. It was found that the wall roughness can significantly influence particle deposition and that particles with diameters larger than 4 μm were trapped by the surface roughness.

To the best of the authors' knowledge, no in-depth investigation has been performed on the deposition patterns of wood dusts in a human nasal cavity. This study therefore investigated the detailed deposition of wood particles in an anatomically accurate nasal cavity using CFD techniques. The nasal cavity was generated from computed tomography (CT) data. Three wood dusts, pine dust, heavy oak dust, and light oak dust, defined by a particle size distribution generated by machining (Chung et al., 2000), were simulated at a flow rate of 10 L/min. The objectives of this study were to identify major deposition regions, to compare the deposition patterns of different wood dusts, and to discuss the clearance mechanism of the deposited dust. The simulated results aimed to contribute to the understanding of particle deposition patterns of different wood dusts and also to assist in risk analysis of wood dust exposure in industries.

METHODS

CT-Based Nasal Cavity Geometry

The nasal cavity geometry was obtained through a CT scan of the nose of a healthy 25-yr-old, Asian male (170 cm height, 75 kg mass). The CT scan was performed using a CTI whole body scanner (General Electric). The single-matrix scanner was used in helical mode with 1 mm collimation, a 40-cm field of view, 120 kV peak, and 200 mA. The scans captured outlined slices in the x–y plane at different positions along the z axis from the entrance of the nasal cavity to just anterior of the larynx at intervals of 1 to 5 mm depending on the complexity of the anatomy. The coronal sectioned scans were imported into a three-dimensional (3D) modeling program called GAMBIT (GAMBIT 2.2, 2004), which created smooth curves that connected points on the coronal sections. Surfaces were then created and stitched up to create a computational mesh. The computational domain was then categorized into 10 different regions. The anterior third of the nasal airway can be regarded as regions 1–4, the middle airway as regions 5–8, and the posterior third is taken as regions 9–10 (Figure 1). A long tubular extension was included in the geometry to avoid any fluctuations at the exit.

Fluid Flow Modeling

Due to the complex geometry of the anatomically real nasal cavity, a commercial CFD code, FLUENT (FLUENT 6.2, 2005), was utilized to predict the continuum gas-phase flow through solutions of the conservation equations of mass and momentum. A steady inhalation flow rather than a cyclic unsteady flow was used in this case to isolate and focus the results on deposition independent from time and fluctuation variables. Additionally the effects of a periodic inhalation on the overall flow field were found to be negligible from the Womersley frequency variable that is used to determine the importance of the fluctuating sinusoidal pattern of the inhalation-exhalation breathing cycle. The calculated Womersley frequency variable,

$$W = \frac{D_l}{2}\left(\frac{\omega}{\nu_g}\right)^{0.5} \quad [1]$$

was 0.3 where D_l is the local cross-sectional distance between the two nasal walls and is about 0.5 cm in this nasal cavity, ν_g is the kinematic viscosity of air, and ω is the breathing frequency with a value of 0.25 s^{-1}. Moreover, Haußermann et al. (2002) compared the particle deposition in a nasal cast for several human breathing patterns with steady inhalation flows. It was shown that the deposition efficiency of a cyclic breathing pattern was similar to that of a steady inhalation flow for a flow rate of 10 L/min, which was the flow rate used in this study (Haußermann et al., 2002).

This study considered a 10 L/min airflow in the nasal cavity as a laminar flow. Experimental studies by Swift and Proctor

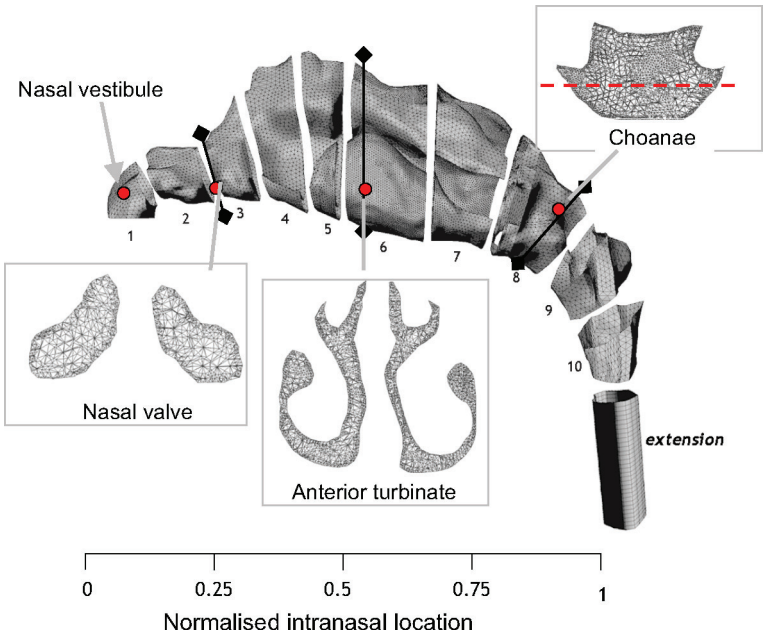

FIG. 1. Computational model with 950,000 cells subdivided into 10 regions to represent local deposition regions. Three coronary sections display the internal mesh where the dashed line across the choanae region is used for grid independence in Figure 3.

(1977) and Kelly et al. (2004) have suggested that a laminar flow regime dominates for low flow rates around 10 L/min. While the Hahn et al. (1993) results also concur, it is mentioned that the flow is a disturbed laminar regime. The authors conducted a literature survey and found that recent numerical simulations in literature have taken the intranasal flows as in a laminar regime for flow rates up to 21 L/min, such as in Naftali et al. (2005), Schroeter et al. (2006), Croce et al. (2006), and Garcia et al. (2007).

The steady-state continuity and momentum equations for the air phase in Cartesian tensor notation are:

$$\frac{\partial}{\partial x_i}\left(\rho_g u_i^g\right) = 0 \qquad [2]$$

$$\rho_g u_j^g \frac{\partial u_i^g}{\partial x_j} = -\frac{\partial p_g}{\partial x_i} + \frac{\partial}{\partial x_j}\left(\mu_g \frac{\partial u_i^g}{\partial x_j}\right) \qquad [3]$$

where u_i^g is the ith component of the time averaged velocity vector and ρ_g is the air density, p_g is the air pressure, and μ_g denotes the air molecular viscosity.

These equations were discretized using the finite volume approach. The third-order accurate QUICK scheme was used to approximate the momentum equation whilst the pressure-velocity coupling was realized through the SIMPLE method. The convergence criteria for the air phase properties (resolved velocities and pressure) were set at 10^{-5}. The sufficiency of the convergence criteria was further checked by comparing the simulation of airflows along a line at the choanae section (Figure 1) with the convergence criteria values of 10^{-5} and 10^{-7}. The difference of air velocity profile between the two simulations was negligible.

Particle Trajectory Modeling

There are generally two basic categories of computational approaches that are currently used to predict the particle phase flows: the Eulerian two-fluid model and the Lagrangian particle-tracking model. In the Eulerian model, the particle flow is treated as continuous fluid flow and regarded as interacting with the fluid phase. A Lagrangian particle tracking method was therefore used in the current study to trace the dispersion of particles about its trajectory. The Lagrangian scheme is most popular in engineering applications for the prediction of particle flows because of its ability to provide detailed physical description of the particle behaviours by tracking particles individually. Trajectories of individual particles can be calculated by integrating the force balance equations on the particle:

$$\frac{du_p}{dt} = F_D(u_g - u_p) + \frac{g(\rho_p - \rho_g)}{\rho_p} \qquad [4]$$

where u_p presents the particle velocity and ρ_p is the particle density. Equation (4) does not include other forces such as Brownian force and Saffman's lift force. The Brownian force can be neglected, since these effects should only be included for sub-micron particles only (Ounis et al., 1991). Saffman's lift force was not included due to relatively large particles and low-level fluid turbulence. Zhang et al. (2002b) confirmed these assumptions in validating the particle deposition results in a triple bifurcation lung airway model with experimental results.

The term$F_D(u_g - u_p)$ in Eq. (4) is the drag force per unit particle mass and F_D is given by:

$$F_D = \frac{18\mu_g}{\rho_p d_p^2}\frac{C_D \mathrm{Re}_p}{24} \quad [5]$$

where d_p is the particle volume equivalent diameter. Re_p is the particle Reynolds number, which is defined as:

$$\mathrm{Re}_p \equiv \frac{\rho_p d_p |u_g - u_p|}{\mu_g} \quad [6]$$

It is noted that the gravity term g was taken as –9.81 m/s^2 taken in the y axis and hence is applicable for an upright position.

The drag coefficient C_D is given by Morsi and Alexander (1972) as:

$$C_D = a_1 + \frac{a_2}{\mathrm{Re}_p} + \frac{a_3}{\mathrm{Re}_p^2} \quad [7]$$

where the a tems are empirical constants for smooth spherical particles over several ranges of particle Reynolds number.

Wood Dust Simulations

Dusts from pine (softwood) and from light and heavy oak (hardwood) were simulated where their respective densities are 560 kg/m^3, 590 kg/m^3, and 930 kg/m^3. A study carried out by Chung et al. (2000) examined the particle size distribution of dusts during sawing and sanding of pine and oak. Oak dust generated by sawing exhibited smaller particle sizes than the pine dust, while similar size distributions were found for both pine and oak dust when generated by sanding. Therefore, only intranasal depositions of wood dust with size distributions from sawing were investigated herein. Figure 2 illustrates the measured and simulated particle size distribution of both pine and oak. It is noted that the particle size distributions in Figure 2 were based on the particle number fraction and not volume fraction nor mass fraction. Both heavy oak dust and light oak dust were assumed to have the same size distribution. All particles in this study were assumed to be spherical.

The equivalent aerodynamic diameter, d_{ae}, is defined as

$$d_{ae} = d_p\sqrt{\rho_p/1000} \quad [8]$$

In still air, particles with d_{ae} that are smaller than 1 μm are likely to be found suspended in the air, while particles with d_{ae} from 1 μm to 10 μm tend to settle by gravity. However, normal air movements that are typically found in indoor workshops have been shown to make all particles suspend in the air for a long period of time. This includes particles with d_{ae} larger than 10 μm that have been found suspended in the air near the dust source and under strong wind conditions (ASHRAE, 2001). Moreover, the study of the inhalability of ultralarge particles in still air conducted by Dai et al. (2006) confirmed that the "cut-off" particle size for nasal inhalation is approximately 135 μm. Therefore, particles with d_{ae} of 10 μm and greater were also considered for investigation for the case of wood dust deposition

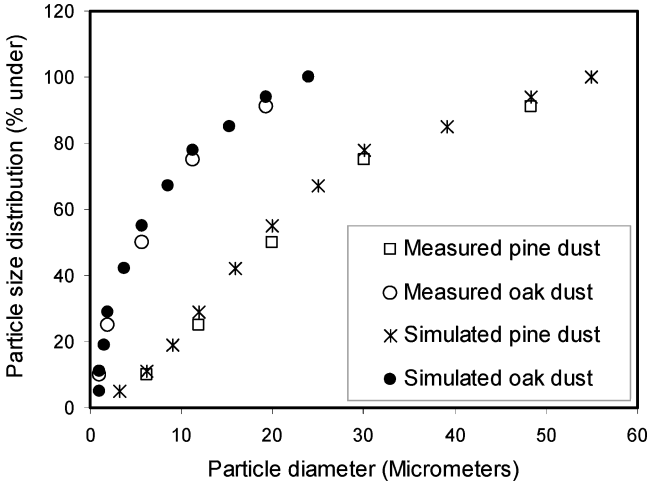

FIG. 2. Simulated particle size distribution and measured particle size distribution of dusts generated by sawing (From Chung et al. 2000).

when the dust source is near, such as the common scenario of wood workshops and other secondary wood industries. For pine dust with density of 560 kg/m^3 and size range of 3–55 μm, this equates to a range of 2–41 μm. For oak dusts with a size distribution from 1 μm to 24 μm, the corresponding d_{ae} is 0.94 to 23 μm for heavy oak while the d_{ae} range is 0.76 to 19 μm for light oak.

In this study, three particle deposition efficiencies were used to quantitatively present the simulation results: the total deposition efficiency η_{total}, the regional deposition efficiency $\eta_{n,regional}$, and the cumulative deposition efficiency $\eta_{n,cumulative}$. The total deposition efficiency η_{total} is defined as:

$$\eta_{\mathrm{total}} = \frac{N_{totaldep}}{N_{totalin}} \times 100\% \quad [9]$$

Here, $N_{totaldep}$ is the total number of particles deposited in the whole nasal cavity while $N_{totalin}$ is the total number of particles released at the nostrils.

The regional deposition efficiency for the nth region (regional numbers are shown in Figure 1), $\eta_{n,regional}$, is calculated as:

$$\eta_{\mathrm{n,regional}} = \frac{N_{n,depo}}{N_{totalin}} \times 100\% \quad [10]$$

Here, $N_{n,depo}$ is the number of particles deposited in the nth region.

The cumulative regional deposition efficiency for the nth region, $\eta_{n,cumulative}$, is given as

$$\eta_{n,cumulative} = \sum_{\mathrm{i=1}}^{\mathrm{n}} \eta_{\mathrm{i,regional}} \quad [11]$$

Boundary Conditions

For the air phase simulation, uniform velocity profiles at a flow rate of 10 L/min were used at the nostrils entrances. Though

the flows at the entrance to nostril were fully developed in some experimental studies, it has been found that a given nostril airflow does not have significant influence on the downstream flow patterns (Keyhani et al., 1995; Shi et al. 2007). A pressure outlet boundary condition was used at the end of the extension (Figure 1) and a gauge pressure was set to zero.

In a previous study by Inthavong et al. (2006), the influence of u^*, the ratio of particle initial velocity to gas phase inlet velocity, on the spray particle deposition in nasal cavity was investigated numerically. It is found that the deposition of 10–20 μm spray particles was only sensitive to high values of u^* ($u^* \approx 10$). However, the wood dust inlet velocity is naturally close to or slower than the inhaled air velocity, i.e., u^* is equal to or less than unity. The deposition efficiency of pine dusts with different u^* from 0 to 1 were simulated and the differences were found to be negligible. In all simulations within this study, particles were released space evenly at the entrances of nostrils with the air flow velocity, thus assuming that the particles are suspended in the air.

The nasal cavity wall was set to "trap" in particle boundary condition based on the assumption that the wall is usually wet, so that once a particle hits the wall it would be trapped and determined as having deposited.

Definition of Stokes Number and Inertial Parameter

For gas-particle flows, the dimensionless Stokes number is defined as the ratio between the particle relaxation time and the average residence time of particles in the nasal cavity:

$$St = t_p / t_s \quad [12]$$

This equation presents an important criterion toward understanding the state of the particles and whether they are in kinetic equilibrium with the surrounding gas (Tian et al., 2005). The particle relaxation time is defined as:

$$t_p = \frac{\rho_p d_p^2}{18\mu_g} \quad [13]$$

The average residence time of particles t_s in the Stokes number definition is determined from the characteristic length (D) and the characteristic velocity (U) normally taken as the air phase inlet value,

$$t_s = D/U \quad [14]$$

The Stokes number is a measure of the influence of the inertial effects during a particle's trajectory. However its application is dependent on the characteristic length that varies between different nasal cavity geometries. Instead, the inertial parameter I given by

$$I = Qd_{ae}^2 \quad [15]$$

may be used as it uses the airflow rate, Q, to normalize out the characteristic length and the air-phase velocity. It is a convenient parameter that compares deposition against different flow rates and particle sizes at aerodynamic diameters, although its only drawback is its use of a constant flow rate, which doesn't take into account the airway geometry. Despite this, it is widely used for presenting particle deposition efficiencies, especially for in vivo data, where it is difficult to determine an adequate characteristic length for realistic human airways.

RESULTS AND DISCUSSIONS

First, a three-step quality control procedure was implemented to ensure the reliability of numerical simulation results in this study. This procedure included (1) a mesh independence test, (2) qualitative validation of air phase simulation by streamline analysis, and (3) quantitative comparison of total deposition efficiency of monodispersed pine particles with other experimental and numerical results.

Mesh Independence Test and Air-Phase Streamline Analysis

An initial mesh with 82,000 cells was created from the CT-based nasal cavity, which was refined by cell adaptation techniques that included refining large-volume cells, cells that displayed high velocity gradients, and cells near wall refinements. This process was repeated 3 times, resulting in 4 models with mesh densities of 82,000, 586,000, 950,000, and 1.44 million cells. Figure 1 shows the mesh density of 950,000 cells with 3 coronary slices showing the internal mesh with a dense region near the walls. Mesh independence was checked by comparing the air-phase velocity magnitude along a line at the choanae section (Figure 1) computed using different mesh densities. Figure 3a illustrates the comparison of air velocity magnitude obtained from 82,000, 950,000, and 1.44 million cells. The fine mesh density of 1.44 million and medium mesh density of 950,000 cells yield almost identical results, indicating that mesh convergence was achieved. Additionally, to investigate the effects of mesh resolution near the wall on particle deposition, the total particle deposition efficiency of 2 mesh densities, 950,000 and 1.44 million cells,were compared. Cells close to the wall boundaries were adapted from the former mesh density to the latter mesh density. The difference of the total particle deposition efficiencies of both mesh densities was found to be negligible (Figure 3b). The mesh density of 950,000 cells was therefore applied.

The air-phase prediction is essential for particle deposition prediction, since particle dispersion and transportation are strongly affected by the air-phase velocity. Therefore, qualitative validation of the airflow in this nasal cavity was carried out by analysing the streamlines. Figure 4 shows the streamlines passing through different velocity contours within the nasal cavity. Air enters the nostril inlet at a velocity of 1 m/s and accelerates as it squeezes through a narrowing region called the nasal valve, and a maximum velocity of 2.18 m/s is reached in this region (Section A–A′). This acceleration and high velocity region enhance a particle's impactability. Beyond the nasal valve the nasal airway expands and the air experiences a sharp deceleration. Regions of low flow and recirculation are found in the upper regions

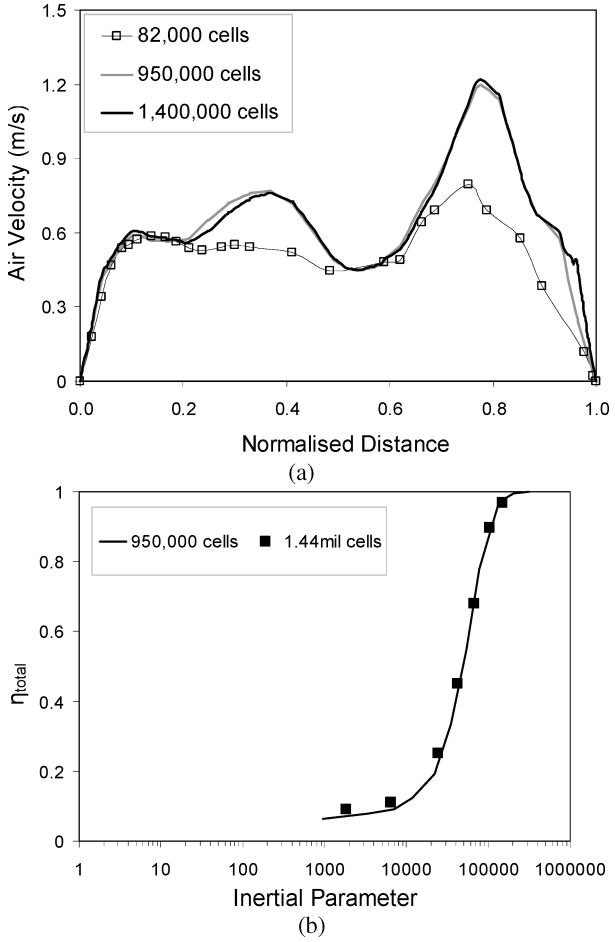

FIG. 3. (a) Grid independence test based on a velocity profile taken at the choanae section shown in Figure 1. (b) Grid independence test on deposition of particles for two refined nasal cavity models.

of Section B–B′ known as the olfactory region. From the inlet the streamlines separate into three main regions of flow: The air entering from the anterior tip of the nostril was found to flow through the olfactory region and the middle meatus, while the air originating from the posterior part of nostril flowed through the middle and inferior meatus. Simulations by Zamankhan et al. (2006) and Subramanian et al. (1998) also noted similar flow paths as well as regions of recirculation. A closer investigation revealed that the majority of air passed through the middle meatus on the septum side of the nasal cavity and along the floor of the airway highlighted by the light colours in Section C–C′. The division of air after the nasal valve expansion was also observed by Hahn et al. (1993) where it was found that 50% of the inspired air flowed through the combined middle and inferior airway, while 14% through the upper olfactory region. At Section D–D′ the flow becomes more uniform as the left and right sides of the geometry begin to merge and the cross-sectional area widens. At the nasopharynx (Section E–E′) the left and right cavities have merged into one enlarged conduit and the airflows from both cavities meet, creating intense mixing.

Total Deposition Efficiency of Monodisperse Pine Particles

The total deposition efficiencies of monodisperse pine particles were simulated for 11 particle sizes, $d_p = 3$, 6.2, 9.1, 11.9, 16, 20, 25, 30, 39.2, 48.3, and 55 μm, respectively. For each particle size, 11,700 monodisperse particles were released spaced evenly from both nostrils with zero initial velocity. Figure 5 compares the predicted total deposition efficiency, η_{total}, with other experimental investigations (Pattle, 1961; Kelly et al., 2004) and numerical results (Shi et al., 2007).

The current CFD techniques captured the trend of total deposition efficiency by predicting the curve reasonably. The differences in deposition may be attributed to the intersubject variability between the nasal cavity models obtained by Kelly et al. (2004) (53-yr-old nonsmoking Caucasian male) and the model used in the present study (25-yr-old Asian male), while Häußermann (2001) also states that nasal cavity replicate casts with wider airways can cause less deposition due to secondary flow. Furthermore, Kelly et al. (2004) point out that differences in comparison of particle inertial deposition with different nasal cavity models can be explained by inertial impaction considerations. For $d_{ae}^2 Q$ values less than 2000 μm^{2}cm^3/s, particles have a shorter relaxation time, which allows the particles to adjust to flow streamlines more readily and hence the effect of different geometries is less significant. Accordingly the comparison between the deposition curve of the CFD simulation and the experimental data is fairly similar at this lower range. As the value of $d_{ae}^2 Q$ increases, the particles' relaxation time increases and the particles are more likely to continue their own trajectory, deviating from a curving streamline. The differences in geometries that cause curvatures in streamlines are therefore more significant for larger inertial particles and greater deviation between different geometries is reasonable. Therefore, when neglecting the experimental uncertainties and differences in geometry, the characteristics of the CFD results correspond to the experimental data reasonably well. In summary, the results show that the current CFD model setting is sufficient to provide tolerable accurate information in terms of fluid-particle dynamics and particle deposition in a realistic human nasal cavity.

Deposition Patterns of Polydisperse Wood Dust Particles

Deposition patterns of polydisperse pine and oak dusts representing particle size distribution generated by sawing (Figure 2) were simulated. For each dust, 11 groups of monodisperse particles with different particle numbers according to its distribution were combined to represent the particle size distribution measured by Chung et al. (2000). Table 1 lists the particle numbers for each group of monodisperse particles. For each size group, a "particle injection" boundary condition for the Lagrangion model was generated in FLUENT to initialize the particle positions spaced evenly at both nostril inlets. The 11 "particle

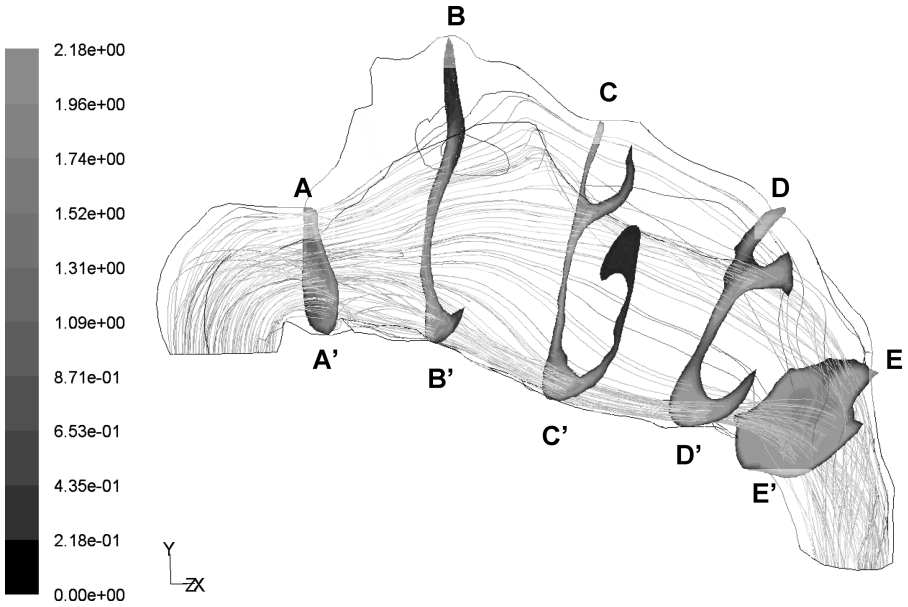

FIG. 4. Air flow streamlines passing through velocity contours taken at different coronal sections in the right nasal cavity.

injections" were then released simultaneously. The total number of particles for each polydisperse injection was 11,700.

Figure 6a compares the regional deposition efficiency of dusts, $\eta_{n,regional}$, in different intranasal regions (shown in Figure 1), while Figure 6b gives the cumulative regional deposition efficiency, $\eta_{n,cumulative}$. Figure 7 displays the deposition patterns of different dusts in the nasal cavity. It can be seen that the anterior nasal segment (region 1–4) was the most dominant region of particle deposition for all wood dusts. This is consistent with experimental observations of Fry and Black (1973). In between regions 2 and 3 lies the nasal valve that plays a major role in particles depositing in the anterior nasal segment, in that it has the smallest cross-section area. The nasal valve accounts for approximately half of the total airway resistance and has been considered a major obstruction to the delivery of inhaled pharmaceuticals by nasal spray (Schroeter et al., 2006). Beyond the nasal valve, particles depositing in region 3 (Figure 7) occur on the septum walls of both sides of the cavity. The second highest concentration of particle deposition of all wood dusts is found on the anterior parts of the middle turbinates in region 6, while a small proportion of particles deposited at the back of the nasal cavity, where the flow changes directions from horizontal to vertically downwards. The change in the flow direction at

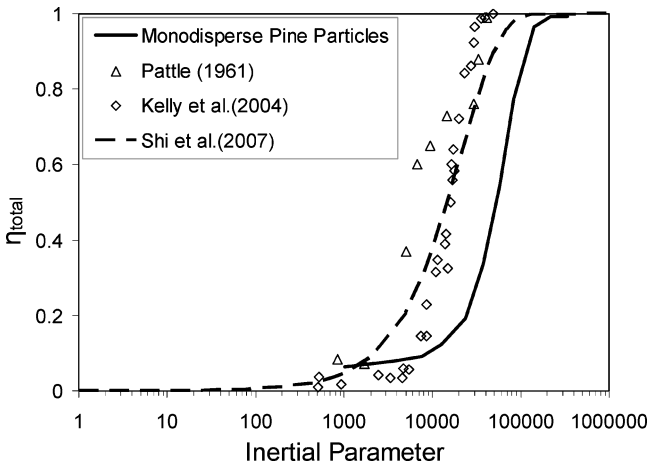

FIG. 5. CFD simulation results for total deposition efficiency (DE) of monodisperse pine particles compared with other experimental and numerical results.

TABLE 1
Simulated particle numbers for pine and oak dusts representing particle size distribution generated by sawing

Particle Size (μm)		Particle size distribution (%)	Simulated particle number
Pine dust	Oak dust		
3	1	5	600
6.2	1.2	6	750
9.1	1.5	8	900
11.9	1.9	10	1200
16	3.8	13	1500
20	5.7	13	1500
25	8.5	13	1500
30	11.3	10	1200
39.2	15.3	8	900
48.3	19.3	9	1050
55	24	5	600
Total		100	11700

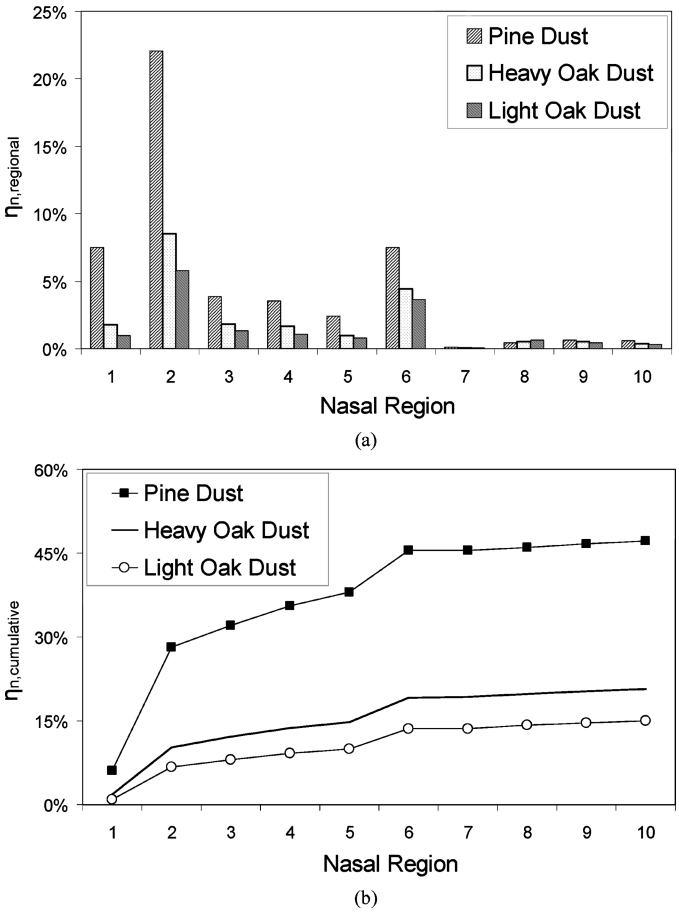

FIG. 6. (a) Local DE of all dusts; (b) Cumulative local DE of all dusts.

the nasopharyngeal region again acts like an inertial impactor, filtering out high-inertial particles. Pine dust had much higher deposition efficiency than oak dusts in the anterior nasal segment, as it comprised much larger particles. On the other hand, oak dusts consisting of smaller particles lead to a lower deposition. Compared with heavy oak dust, light oak dust had a lower deposition efficiency, although it had the same particle distribution as heavy oak dust. This was due to a lower material density that light oak dust exhibits and consequently a lower Stokes number.

The effects of deposition on the anterior parts of the middle turbinates (second highest concentration) of the nasal mucous membrane have been found to cause pathological changes in the nose, such as squamous metaplasia of the mucous membrane covering the anterior ends of the middle turbinate (Hadfield, 1972). This local region of deposition suggests that the natural filtration ability of the nasal airway in the region anterior of the nasal valve prevents only the higher inertial particles. In a study of wood dust deposition in the nose of furniture workers (Hadfield, 1972), wood particles were found to accumulate in two major regions: (1) in a small, oval-shaped area on the anterior part of the nasal septum near the floor of the nose, and (2) on the anterior part of the middle turbinate. It is noticeable that these regions also exhibit high particle deposition efficiency in the current CFD study. Inhaled wood dust depositing on these regions is retained and any toxic substance that it may contain remains in contact with this part of the epithelium for a longer time than on other regions, which are covered by ciliated epithelium (Fry & Black, 1973), and therefore damages the exposed layer of soft tissues. This has been confirmed by observations of Hadfield (1973), where the deposited particles washed away from the anterior end of the middle turbinate for a large number of furniture workers under investigation produced a rough granular appearance to the naked eye, which could be surmised as a premalignant lesion.

The contribution of deposition in the anterior regions by nasal hairs was not considered as they did not appear on the CT scanning. Nevertheless, it has been found that the absence of the nasal hairs did not affect the intranasal airflow and particle deposition efficiency significantly (Hahn et al., 1993; Swift & Kesavanathan, 1996).

Particle Size Fraction Analysis of Deposited Dusts

The particle size fractions of deposited polydisperse pine particles and polydisperse light oak particles were analyzed. Here, the fraction of particles with a size of d_p deposited in the nth region, $F_{n,dp}$, is defined as

$$F_{n,dp} = \frac{N_{n,dp}}{N_{n,depo}} \times 100\% \qquad [16]$$

where $N_{n,dp}$ is the number of particle with a size of d_p deposited in the nth region. and $N_{n,depo}$ is the number of particles deposited in the nth region.

Figure 8, a and b, shows the particle size fraction of deposited pine dust and light oak dust, respectively. In Figure 8a, larger particles ($d_p \geq 16$ μm) account for a large proportion of regional deposition in regions 1–5. Larger particles exhibit higher Stokes numbers, which prevents the particles from following the curved streamlines. As a result, most large particles deposit in the regions 1–5 due to nasal valve and curved geometry where flow suddenly changes direction. Particles smaller than 20 μm account for a very small proportion of deposition in these regions due to the particles' ability to follow the airflow. In region 6, most deposited particles were in the range of 16–48 μm. It is observed that there is a reduction in the deposition of 55 μm particles, since most 55 μm particles had already deposited in regions 1–5. A similar trend can be found for light oak dust in Figure 8b, where deposition of large particles ($d_p \geq 16$ μm) were dominant in regions 1–6, while medium-size particles had high deposition concentrations in regions 7–10.

Besides the particle size distribution of the pine and oak dusts generated by sawing, Chung et al. (2000) also measured the mean particle size of the pine and oak wood dust to be 18.6 μm and 4.9 μm, respectively. Figure 9 compares the cumulative regional deposition efficiency of polydisperse pine and heavy

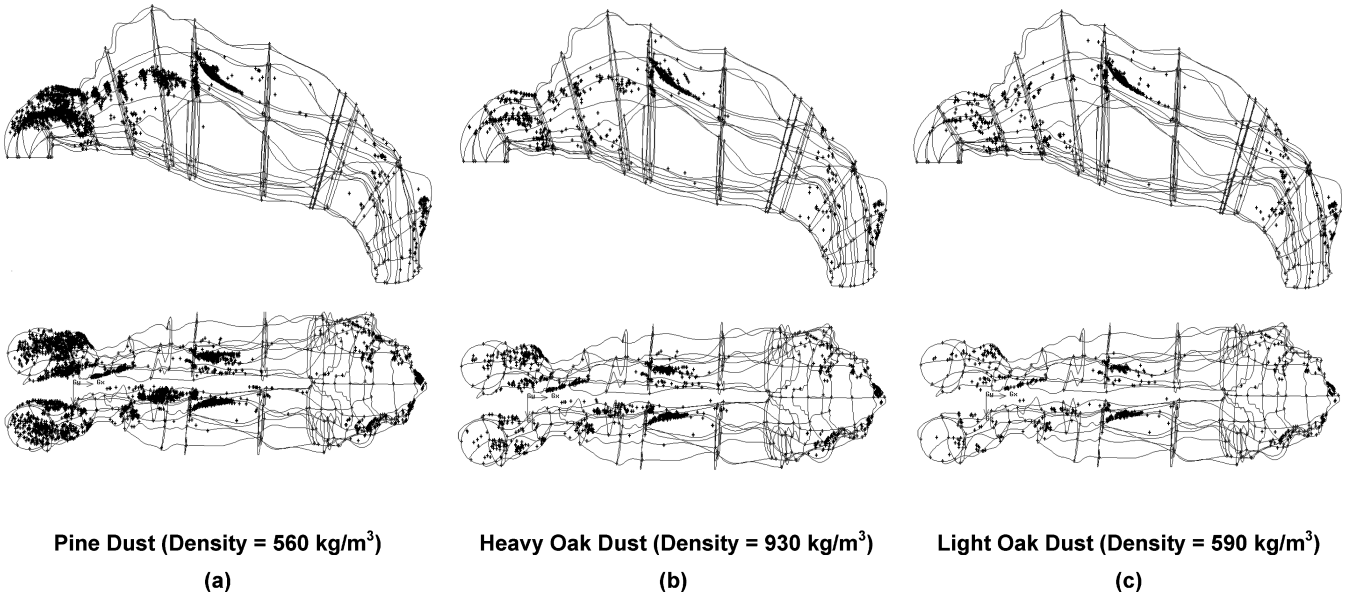

FIG. 7. Local deposition patterns of wood dusts with different particle size distributions.

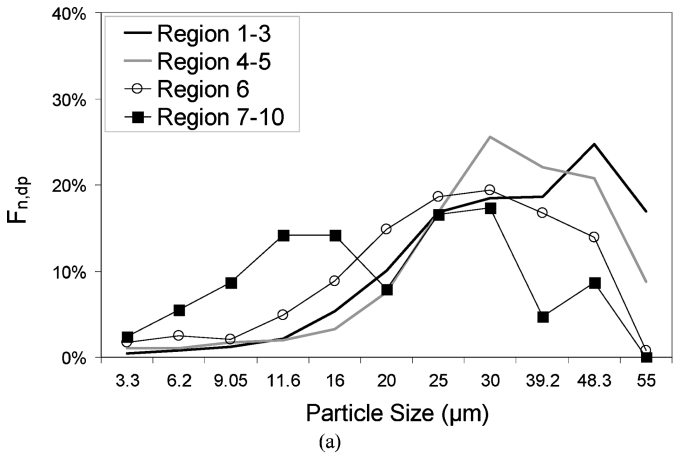

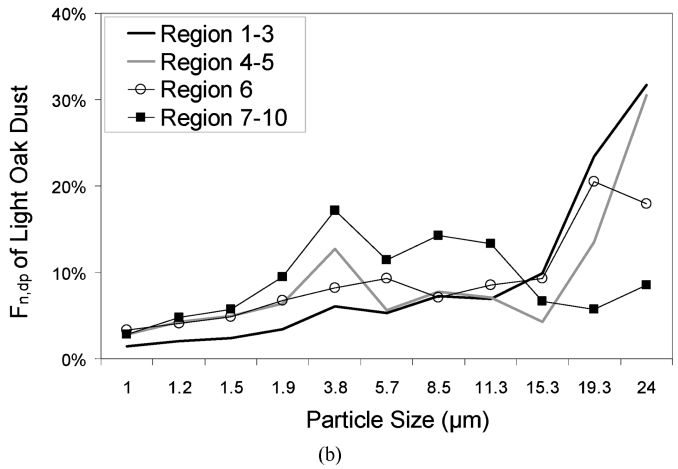

FIG. 8. Particle size distribution (PSD) of deposited particles: (a) Pine dust; (b) Light oak dust.

oak particles against that of monodisperse particles with size of 18.6 μm for pine particles and 4.9 μm for heavy oak particles. The polydisperse injection method for pine and heavy oak particles representing the size distributions generated by sawing was used, with the details of the particle injections having been discussed in the previous section. For 18.6 μm pine particles and 4.9 μm heavy oak particles representing the mean particle size of the pine and oak wood dust, 11,700 monodisperse particles were released spaced evenly from both nostrils with zero initial velocity. It is clear that the deposition using a polydisperse size distribution is much higher than the mean particle deposition efficiency, indicating that the mean particle diameter is not suitable for representative deposition studies.

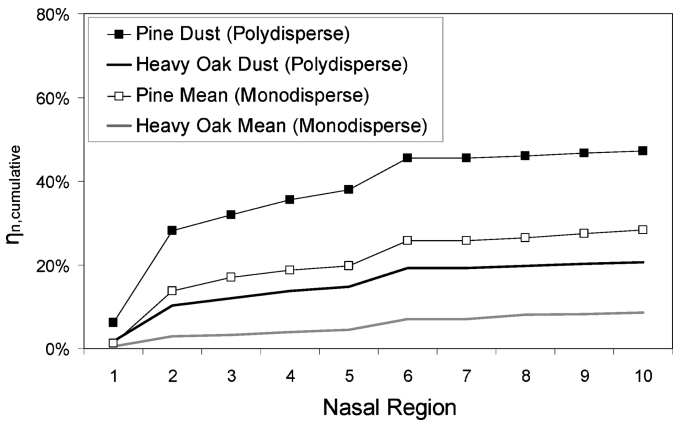

FIG. 9. Cumulative local DE of pine and heavy oak dusts and monodisperse mean particles.

CONCLUSIONS AND FUTURE WORK

Wood dust deposition in a CT-based nasal cavity was simulated using CFD techniques, and the following conclusions can be drawn. First, the major particle deposition sites include the nasal valve region and anterior section of middle turbinate. Wood dust deposited in these regions was removed more slowly and the layer of soft tissues in these regions may be damaged by the continuous exposure to wood particles. Second, it was found that pine dust had high deposition efficiency in the nasal cavity in comparison with heavy and light oak dusts, due to the fact that it comprised much larger particles. On the other hand, this indicates that dusts with a large amount of fine particles, such as dusts generated by fine sanding, may penetrate the nasal cavity and travel further into the lung. Third, large wood particles ($d_p \geq 16\ \mu$m) account for a large proportion of deposited dust in region 1–6, while particles with medium size were dominant in region 7–10. Finally, the deposition efficiency of monodisperse particles with a mean particle size is not suitable to represent the deposition efficiency of the wood dust, which exhibits a particle size distribution.

Haußermann et al. (2002) pointed out that breathing patterns had significant influences on the particle deposition when flow rates were higher than 10 L/min. Wiesmiller et al. (2003) also demonstrated that intranasal particle deposition takes place during inhalation as well as during exhalation. Additionally, all dust particles in this study were assumed to be spherical, but wood dusts in industrial environment exhibit different morphology, which may undermine the aerodynamic properties of the particles. Therefore, future work is still required to assess the influence of breath patterns at higher flow rates and particle morphology on the deposition of wood dust in the nasal cavity.

REFERENCES

ASHRAE. 2001. Ventilation and infiltration. In *ASHRAE handbook 2001, Fundamentals*, Chapter 26. Atlanta, GA: American Society of Heating, Refrigeration and Air Conditioning Engineers.

Cheng, K. H., Cheng, Y. S., Yeh, H. C., Guilmette, R. A., Simpson, S. Q., Yang, Y. H., and Swift, D. L. 1996. In vivo measurements of nasal airway dimensions and ultrafine aerosol deposition in the human nasal and oral airways. *Aerosol Sci.* 27(5):785–801.

Chung, K. Y. K., Cuthber, R. J., Revell, G. S., Wassel, S. G., and Summer, N. 2000. A study on dust emission, particle size distribution and formaldehyde concentration during machining of medium density fibreboard. *Ann. Occup. Hyg.* 44:455–466.

Croce, C., Fodil, R., Durand, M., Sbirlea-Apiou, G., Caillibotte, G., Papon, J.-F., Blondeau, J.-R., Coste, A., Isabey, D., and Louis, B. 2006. In vitro experiments and numerical simulations of airflow in realistic nasal airway geometry, *Ann. Biomed. Eng.* 34(6):997–1007.

Dai, Y. T., Juang, Y. J., Wu, Y. Y., Breysse, P. N., and Hsu, D. J., 2006. In vivo measaurements of inhalability of ultralarge aerosol particles in calm air by humans. *J. Aerosol Sci.* 37:967–973.

Enarson, D. A., and Chan-Yeung, M. 1990. Characterization of health effects of wood dust exposures. *Am. J. Ind. Med.* 17:33–38.

Finck, M., Hänel, D., and Wlokas, I. 2007. Simulation of nasal flow by lattice Boltzmann methods. *Comp. Biol. Med.* 37:739–749.

FLUENT, Inc. 2005. *FLUENT 6.2 documentation*. Lebanon, NH: FLUENT, Inc.

Fry. F. A., and Black, A. 1973. Regional deposition and clearance of particles in the human nose. *Aerosol Sci.* 4:113–124.

GAMBIT. 2004. *GAMBIT 2.2 documentation*. Lebanon, NH: FLUENT, Inc.

Garcia, G. J. M., Bailie, N., Martins, D. A., and Kimbell, J. S. 2007 Atrophic rhinitis: A CFD study of air conditioning in the nasal cavity. *J. Appl. Physiol.* doi:10.1152/japplphysiol.01118.2006.

Guilmette, R. A., Cheng, Y. S., Yeh, H. C., and Swift, D. L. 1994. Deposition of 0.005.12 μm monodisperse particles in a computer-milled, MRI-based nasal airway replica. *Inhal. Toxicol.* 6(Suppl. 1):395–399.

Hadfield, E. M. 1972. Damage to the human nasal mucosa by wood dust. In *Inhaled particles III*, ed. W. H. Walton, vol. II, pp. 855–861. Old Working, UK: Unwin Bros.

Hahn, I., Schere, P. W., and Mozell, M. M. 1993. Velocity profiles measured for airflow through a large-scale model of the human nasal cavity. *J. Appl. Physiol.* 75:2273–2287.

Harper, M., and Muller, B. S. 2002. An evaluation of total and inhalable samples for the collection of wood dust in three wood products industries. *J. Environ. Monit.* 4:648–656.

Häußermann, S., Bailey, A. G., Bailey, M. R., Etherington, G., and Youngman, M. 2002. The influence of breathing patterns on particle deposition in a nasal replica cast. *J. Aerosol Sci.* 33:923–933.

Heyder, J., and Rudolf, G. 1977. Depostion of aerosol particles in the human nose. In *Inhaled particles IV*, ed. W. H. Walton, pp. 107–125. Oxford: Pergamon Press.

Hounam, R. F., Black, A., and Walsh, M. 1971. Deposition of aerosol particles in the nasopharyngeal region of the human respiratory tract. *J. Aerosol Sci.* 2:341–352.

International Agency for Research on Cancer (IARC). 1995. Wood dust. *IARC Monogr. Eval. Carcinogen. Risks Hum.* 62:35–215.

International Agency for Research on Cancer/World Health Organization (IARC/WHO). 1995. Wood dust and formaldehyde. *IARC Monogr. Eval. Carcinogen. Risks Hum.* 62.

Inthavong, K., Tian, Z. F., Li, H. F., Tu, J. T., Yang, W., Xue, C. L., and Li, C. G. 2006. A numerical study of spray particle deposition in a human nasal cavity. *Aerosol Sci. Tech.* 40:1034–1045.

Keck, T., Leiacker, R., Klotz, M., and Lindemann, J. 2000. Detection of particles within the nasal airways during respiration. *Eur. Arch. Oto-Rhino-Larygol.* 257:493–497.

Kelly, J. T., Asgharian, B., Kimbell, J., and Wong, B. A. 2004. Particle deposition in human nasal airway replicas manufactured by different methods. Part I: Inertial regime particles. *Aerosol Sci. Technol.* 38:1072–1079.

Keyhani, K., Scherer, P.W., and Mozell, M.M. 1995. Numerical simulation of airflow in the human nasal cavity. *J. Biomech. Eng. ASME* 117:429–441.

Martonen, T. B., Zhang, Z., Yue, G., and Musante, C. J. 2002. 3-D particle transport within the human upper respiratory tract. *J. Aeros. Sci.* 33:1095–1110.

Morsi, S. A., and Alexander, A. J. 1972. Investigation of particle trajectories in 2-phase flow systems. *J. Fluid Mech.* 55:193–208.

Naftali, S., Roenfeld, M., Wolf, M., and Elad, D. 2005. The air-conditioning capacity of the human nose. *Ann. Biomed. Eng.* 33:545–553.

National Toxicology Program, 2005. *Wood dust, Report on carcinogens*, 11th ed. Washington, DC: U.S. Department of Health and Human Services, Public Health Service.

Pattle, R. E. 1961. The retention of gases and particles in the human nose. In *Inhaled particles and vapors*, ed. C. N. Davies, pp. 302–309. Oxford, UK: Pergamon Press.

Schroeter, J. D., Kimbell, J.S., and Asgharian, B. 2006. Analysis of particle deposition in the turbinate and olfactory regions using a human nasal computational fluid dynamics model. *J. Aerosol Med*. 19:301–313.

Shi, H.W., Kleinstreuer, C., and Zhang, Z. 2007. Modeling of inertial particle transport and deposition in human nasal cavities with wall roughness. *J. Aerosol Sci.,* 38:398–419.

Subramaniam, R. P., Richardson, R. B., Morgan, K. T., and Kimbell, J. S. 1998. Computational fluid dynamics simulations of inspiratory airflow in the human nose and nasopharynx. *Inhal. Toxicol.* 10:91–120.

Swift, D. L. 1991. Inspiratory inertial deposition of aerosols in human nasal airway replicate casts: Implication for the proposed NCRR lung model. *Radiat. Prot. Dosim*. 38(1/3):29–34.

Swift, D. L., and Proctor, D. F. 1977. Access of air to the respiratory tract. In *Respiratory defence mechanism*, eds. J. D. Brain, D. F. Proctor, and L. M. Reid, pp. 63–93. New York: Marcel Dekker.

Tian, Z. F., Tu, J. Y., and Yeoh, G. H. 2005. Numerical simulation and validation of dilute gas-particle flow over a backward-facing step. *Aerosol Sci. Technol*. 39:319–332.

Wiesmiller, K., Keck, T., Leiacker, R., Sikora, T., Rettinger, G., and Lindemann, J. 2003. The impact of expiration on particle deposition within the nasal cavity. *Clin. Orthop. Relat. Res*. 28:304–307.

Zamankhan, P., Ahmadi, G., Wang, Z., Hopke, P. K., Cheng, Y. S., Su, W. C., and Leonard, D. 2006. Airflow and deposition of nanoparticles in a human nasal cavity. *Aerosol Sci. Technol*. 40:463–476.

Zhang, Z., Kleinstreuer, C., Kim, C. S., and Cheng, Y. S. 2004. Vaporizing microdroplet inhalation, transport, and deposition in a human upper airway model. *Aerosol Sci. Technol*. 38:36–49.

Zwartz, G. J., and Guilmette, R. A. 2001. Effect of flow rate on particle deposition in a replica of a human nasal airway. *Inhal. Toxicol*. 13:109–127.